

Stimulated Raman Photothermal Microscopy towards Ultrasensitive Chemical Imaging

Yifan Zhu^{1, #}, Xiaowei Ge^{2, #}, Hongli Ni², Jiaze Yin², Ji-Xin Cheng^{1,2,3,4,*}

Abstract

Stimulated Raman scattering (SRS) microscopy has shown enormous potential in revealing molecular structures, dynamics and coupling in a complex system^{1–3}. However, the bond-detection sensitivity of SRS microscopy is fundamentally limited to milli-molar level due to the shot noise and the small modulation depth in either pump or Stokes beam⁴. Here, to overcome this barrier, we revisit SRS from the perspective of energy deposition. The SRS process pumps molecules to their vibrational excited states. The thereafter relaxation heats up the surrounding and induces a change in refractive index. By probing the refractive index change with a continuous wave beam, we introduce stimulated Raman photothermal (SRP) microscopy, where a >500-fold boost of modulation depth is achieved on dimethyl sulfide with conserved average power. Versatile applications of SRP microscopy on viral particles, cells, and tissues are demonstrated. With much improved signal to noise ratio compared to SRS, SRP microscopy opens a new way to perform vibrational spectroscopic imaging with ultrahigh sensitivity and minimal water absorption.

Introduction

Avoiding the non-resonant background encountered in coherent anti-Stokes Raman scattering (CARS) microscopy, stimulated Raman scattering (SRS) microscopy has become a powerful platform in the field of chemical imaging^{1–3}. In SRS (**Fig. 1a**), two spatial-temporally overlapped laser pulse trains, namely pump and Stokes, coherently interact with Raman-active molecules that resonates at the laser beating frequency, causing a stimulated Raman gain and loss in the Stokes and the pump field, respectively. While providing the same molecular vibrational features to conventional Raman spectroscopy, SRS offers up to 6 orders of speed improvement comparing to spontaneous Raman³. Such speed improvement, together with development of vibrational probes⁵, has enabled many applications, e.g. label-free stimulated Raman histology^{6,7}, nutrient mapping^{8–10}, unveiling altered metabolism in cancer^{11–15}, heterogeneity in microbiome¹⁶, rapid detection of antimicrobial susceptibility¹⁷. Despite these advances, the detection sensitivity of SRS is fundamentally challenged by the small modulation depth (0.1% for a pure liquid) and the shot noise in the pump or Stokes beam^{4,18}, where simply increasing the number of photons can easily exceed the power tolerance of the sample.

Pushing the fundamental limit of SRS sensitivity requires either a reduction of measurement noise, or a boost of SRS signal. On the reduction of SRS measurement noise, efforts focused on using squeezed light, termed “quantum-enhanced SRS”. Signal-to-noise-ratio (SNR) enhancements of 3.6 dB¹⁹ with continuous wave squeezed light, or 2.89 dB²⁰ with pulsed squeezed light

have been demonstrated with no additional perturbation on sample. While the future of this method is bright, it is currently limited by the low squeeze efficiency and decoherence in complex imaging systems. On the boost of SRS signal, different photophysical processes have been utilized to increase the cross-section, hence the signal intensity, including electronic pre-resonance SRS^{21–23}, plasmon enhanced SRS²⁴ and stimulated Raman excited fluorescence²⁵. Very high enhancement factor ($10^4 \sim 10^7$) of SRS signal, and single molecule SRS measurement^{24,25}, have been achieved. However, the requirement of special target molecules or plasmonic nanostructures constrains the scope of applications.

To seek new approaches towards boosting the signal, we revisit the physics of SRS from the perspective of energy transfer from laser fields to the sample. As explored by Cheng and coworkers in 2007 from the perspective of photodamage in CARS imaging²⁶, ~0.08% of the laser power is absorbed by the sample through the simultaneously occurred stimulated Raman gain and loss processes. As illustrated in **Fig. 1b**, when pump and Stokes pulses with appropriate wavelengths interact with Raman-active molecules, the target molecules are pumped to their vibrationally excited states, with the transition energy Ω equals to the beating frequency between the pump and Stokes lasers. Importantly, after SRS excitation, the vibrationally excited molecules relax their vibrational energy quickly through non-radiative decay, and consequently, heat up the surrounding environment, causing a stimulated Raman photothermal (SRP) effect.

Optically detected photothermal microscopy has been

¹Department of Chemistry, Boston University, Boston, MA, 02215, USA. ²Department of Electrical and Computer Engineering, Boston University, Boston, MA, 02215, USA. ³Department of Biomedical Engineering, Boston University, Boston, MA, 02215, USA. ⁴Photonics Center, Boston University, Boston, MA, 02215, USA

[#]Equal contribution

^{*}Corresponding author: jxcheng@bu.edu

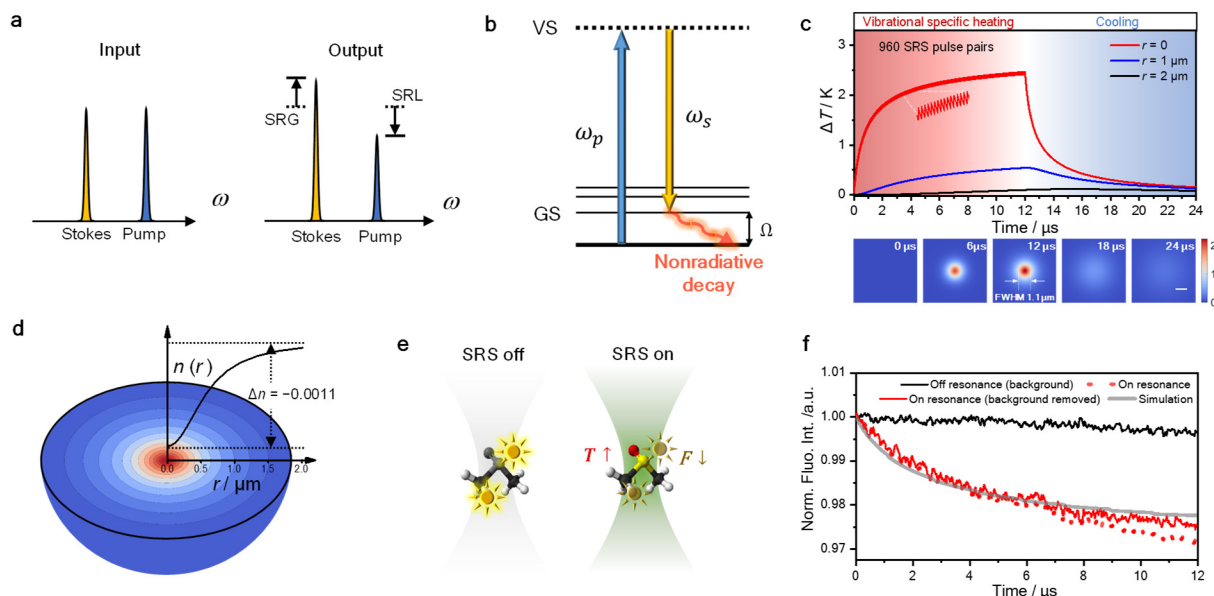


Fig. 1 Theoretical simulation and experimental observation of the SRP effect. **a.** Schematic of stimulated Raman gain and loss. **b.** Schematic of stimulated Raman photothermal (SRP) effect. **c.** Simulation of temperature rise induced by SRP in temporal (top) and spatial (bottom) domains. Spatial scale bar: 1 μm. **d.** Simulated profile of thermal lens induced by SRP in

pure DMSO. **e.** Illustration of fluorescence thermometer measurement of SRP-mediated temperature rise. **f.** Measured fluorescence of rhodamine B in DMSO during an SRS process. The beating frequency (ω_p−ω_s) is tuned to 2913cm^{−1} for on-resonance and 2850 cm^{−1} for off-resonance.

well developed²⁷ and has reached the sensitivity down to a single molecule²⁸. In photothermal spectroscopy, first reported in 1970s²⁹, an optical absorption raises the local temperature, creating local change of refractive index, which is measured with a probing beam. Early photothermal microscopy works focused on electronic absorption, targeting non-fluorescent dye molecules or metal nanostructures²⁷. Recently developed mid-infrared photothermal (MIP) microscopy provides universal infrared active vibrational spectroscopic features, offers a detection sensitivity at micro-molar level, and creates a spatial resolution at the visible diffraction limit^{30,31} or even higher by probing the high harmonic signals³². While MIP microscopy has allowed chemical imaging of living cells, strong water absorption in the infrared region remains a fundamental limitation, which diminishes the infrared pump at a high rate and creates a background at the protein amide I region. In this work, we explore the SRP effect occurring at near-infrared region, where water absorption is negligible.

Simulation of the SRP effect

For a stimulated Raman loss measurement, the relationship between pump beam modulation depth η , pump laser intensity I_p , and change of photon number per pulse, ΔN , can be written as:

$$\eta = \frac{2 \cdot \Delta N \cdot h \omega_p \cdot f_{rep}}{I_p} \quad (1)$$

where h is the Planck's constant, ω_p is the pump

wavenumber, and f_{rep} is the laser repetition rate. With this, one can estimate the energy deposition per pair of SRS pulses by:

$$E = \Delta N \cdot h \omega_R \quad (2)$$

where ω_R is the target Raman shift. Literature⁴ has shown that with 25 mW (modulated at 50% duty cycle) and 15 mW on-sample powers for 80 MHz Stokes and pump beams, respectively, the SRS modulation depth on the 2913 cm^{−1} mode of dimethyl sulfoxide (DMSO) reaches 0.04%. By inserting these measured values into the equations, the energy deposition per pair of laser pulses is found to be 8.7 fJ, equivalent to 0.7 μW.

With this energy deposition estimation, we applied Fourier's law and built a finite unit model (Extended Data Fig. 1) to quantitatively simulate the stimulated Raman induced temperature rise in pure DMSO. Simulation results (Fig. 1c) show that, when using an objective with 0.8 N.A. (numerical aperture), and routinely used laser power (25 mW and 50 mW for pump and Stokes, 80 MHz repetition rate, 50% duty cycle), the temperature rise at the center of the laser focus can reach as high as 2.4 K after 12 μs of stimulated Raman excitation, corresponding to 960 pairs of pump/Stokes pulses. The temperature rises at $r = 1 \mu\text{m}$ and $2 \mu\text{m}$ away from the focal center are 0.54 K and 0.12 K, respectively, at $t = 12 \mu\text{s}$. The temperature map at different time points is also shown in Fig. 1c. The full width at half maximum (FWHM) of the temperature rising field at $t = 12 \mu\text{s}$ is calculated to be 1.1 μm, suggesting a very localized thermal field.

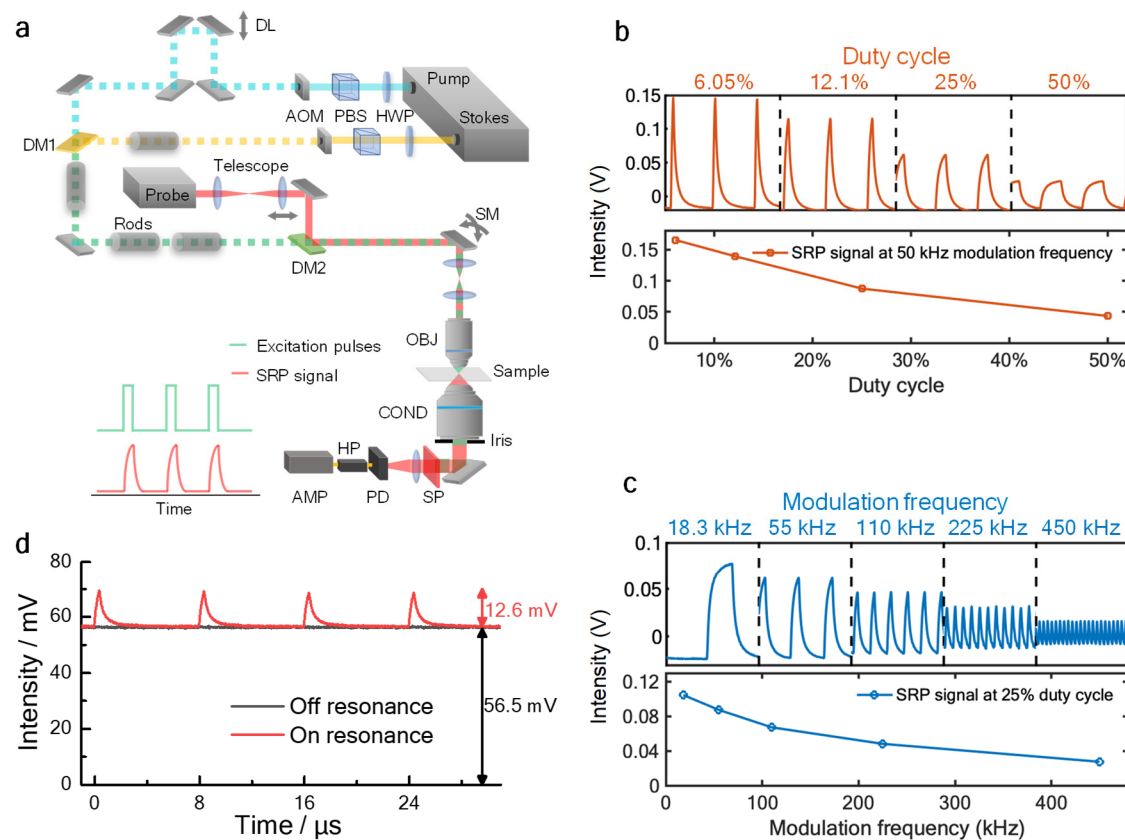


Fig. 2 SRP microscope design and characterization of SRP modulation depth as a function of duty cycle and modulation frequency. **a**. Experimental setup. DM: dichroic mirror; DL: delay line; AOM: acousto-optic modulator; PBS: polarizing beam splitter; HWP: halfwave plate; SM: scanning mirror; OBJ: objective; COND: condenser; SP: spectral filter; PD: photodiode;

HP: highpass filter; AMP: amplifier. **b**. Measured SRP signal as a function of modulation duty cycle. **c**. Measured SRP signal as a function of modulation frequency. **d**. SRP generates a large (22.3%) modulation depth with DMSO as the sample. The on-resonance and off-resonance traces were obtained with the Raman shift at 2913 cm^{-1} and 2850 cm^{-1} , respectively.

The temperature elevation subsequently changes the local refractive index through the thermal-optic effect. For pure DMSO with an index of 1.497 and a thermo-optic coefficient of $-4.93 \times 10^{-4}\text{ K}^{-1} (\partial n / \partial T)^{33}$, at $t = 12\text{ }\mu\text{s}$, the stimulated Raman induced heating causes a refractive index change by -0.07% at the focal center. As shown in **Fig. 1d**, such an index change nonlinearly extends to the surroundings through heat propagation, thus creating a thermal lens. Formation of such a thermal lens builds the foundation for SRP microscopy.

Experimental confirmation of the SRP effect

We experimentally confirmed the simulation results with a fluorescence thermometer. It has been well documented that the emission intensities of some fluorophores is temperature dependent³⁴. For instance, the fluorescence intensity of Rhodamine B decreases by $\sim 2\%$ per Kelvin at room temperature³⁵. This property has been utilized in fluorescence-detected mid-infrared photothermal spectroscopy^{36,37}. Here, we adopt this method to measure the temperature rise at the SRS focus, using Rhodamine B as a fluorescence thermometer. When chirped pump

and Stokes lasers are focused into a DMSO solution of Rhodamine B, the Rhodamine B molecules at the SRS focus are electronically excited to emit fluorescence through multiphoton absorption. Meanwhile, when the beating frequency between pump and Stokes is tuned to resonate with the C-H vibration in DMSO, the SRP effect occurs to raise the temperature and accordingly decrease the two-photon fluorescence intensity of Rhodamine B molecules (**Fig. 1e**).

With this design and identical parameters as in the simulation, we find that the fluorescence intensity drops $\sim 2.3\%$ after $12\text{ }\mu\text{s}$ of on-resonance SRS, corresponding to $\sim 1.2\text{ K}$ of temperature rise (**Fig. 1f**), close to the simulation result of 2.4 K . After weighting each unit in the temperature field with corresponding two-photon excitation intensity of Gaussian beams, the fluorescence change curve can be well fitted as shown in **Fig. 1f**.

A chemical microscope sensing the SRP effect

By sensing the local refractive index modulation using a third continuous wave beam, we have built an SRP

1 microscope as illustrated in **Fig. 2a**. Briefly, the
2 synchronized pump and Stokes pulse trains are intensity-
3 modulated by two AOMs, combined, and chirped to excite
4 the molecules. A probe beam is then collinearly aligned
5 with the SRS beams. A pair of lenses adjusts the
6 collimation of the probe beam to make the probe laser
7 focus axially off the SRS focus, to maximize the
8 photothermal signal²⁷. An iris at the back focal plane of
9 the condenser lens is set to N.A. = 0.4 to convert the
10 probe beam refraction modulation to an intensity
11 modulation. The SRP effect creates a divergent lens,
12 which reduces the effective N.A. of the probe laser focus,
13 thus increases the transmission of the probe beam
14 through the iris. A fast photodiode detects the probe beam
15 intensity, followed by a highpass filter and a broadband
16 amplifier. The SRP modulation induced by synchronized
17 pump and Stokes pulses is digitized in real time by a high-
18 speed digitization card. Details can be found in Methods
19 and Extended Data Fig. 2.

20 Unlike SRS, both pump and Stokes beam are intensity-
21 modulated in the SRP microscope. Since the SRS
22 intensity is proportional to the product of pump and Stokes
23 peak power, with conserved average laser power,
24 reduction of laser duty cycle leads to higher laser peak
25 power, hence more SRS energy deposition. Our
26 experiment (**Fig. 2b**) confirmed this idea and showed
27 much higher SRP signal intensity with lower duty cycle. In
28 SRP imaging applications, the duty cycle was set to 5~10 %
29 as a compromise between signal intensity and laser
30 power. Another key parameter is the modulation
31 frequency. Lower frequency shows higher signal intensity
32 (**Fig. 2c**) due to longer heat accumulation time, but suffers
33 more from the $1/f$ laser intensity noise³⁸ and meanwhile
34 reduces the imaging speed. 125 kHz was chosen to
35 balance these factors.

36 For pure liquid, under 5% duty cycle and 125 kHz
37 modulation frequency, the induced modulation on the
38 probe beam was so strong that we could directly measure
39 the SRP signal in the DC channel without any
40 amplification, as shown in **Fig. 2d**. With reasonable laser
41 powers on sample to excite the C-H symmetric stretching
42 mode (2913 cm^{-1}) of DMSO, the modulation depth
43 reached 22.3%, which is 500-fold higher than the SRS
44 modulation depth (0.04%) with identical average power.
45 The tremendously higher modulation depth builds the
46 foundation for a better detection sensitivity.

47 In addition to duty cycle and modulation frequency,
48 medium is another crucial factor that affects the
49 photothermal signal intensity³⁹. It has been well-
50 formulated that the photothermal signal intensity (Σ_{PT}),
51 thermo-optic coefficient ($\partial n/\partial T$) and heat capacity (C_p)
52 hold the relationship of $\Sigma_{PT}=n(\partial n/\partial T)/C_p$. Yet, the most
53 common medium in biological samples, i.e. water, has a
54 relatively low thermo-optic coefficient ($-1.13\times 10^{-4}\text{ K}^{-1}$)⁴⁰
55 and relatively high heat capacity ($4181\text{ J}\cdot\text{kg}^{-1}\cdot\text{K}^{-1}$). To
56 avoid the signal loss caused by water medium, we
57 investigated a few common liquid media, as shown in
58 Extended Data Table 1. It is found that glycerol maintains

59 the signal intensity very well. Meanwhile, glycerol shows
60 high bio-compatibility, and is widely used as a mounting
61 medium or clearing agent in bio-imaging. Our simulation
62 of the thermal lens comparison, shown in Extended Data
63 Fig. 4, also agrees with the previous theory that the peak
64 refractive index change in glycerol medium is ~2.5-fold as
65 high as in water, with identical heat source (100 nm
66 PMMA nanoparticle under on-resonance SRP heating).
67 Therefore, glycerol was chosen as the medium in
68 following SRP experiments except for the liquid samples.
69 Also, considering the Raman-active vibrational features of
70 glycerol itself, deuterated glycerol (glycerol-d8) was
71 applied for SRP measurement at the C-H and fingerprint
72 regions.

73 Limit of detection and spatial resolution

74 We characterized the performance of our SRP
75 microscope with well-defined samples. We first measured
76 the limit of detection (LOD) for DMSO, focusing on the
77 2913 cm^{-1} mode. To keep the thermal and optical
78 properties constant throughout the measurement,
79 deuterated DMSO (DMSO-d6) was used as the solvent to
80 dilute DMSO. As shown in **Fig. 3a** (and Extended Data
81 Fig. 5 for complete measurement), the SRP spectrum was
82 clean and smooth with high concentration DMSO, and the
83 signal was observable with concentration as low as 15.4
84 mM. We calculated the LOD with the equation of $LOD =$
85 $3\sigma/k$, where σ is the standard deviation of the baseline,
86 and k is the slope of the intensity-concentration linear
87 calibration curve. Calculation yielded a sub-millimolar
88 level LOD value of 0.93 mM. In comparison, the LOD by
89 SRS under identical average laser powers was found to
90 be 39 mM. Thus, SRP measurement offers a ~40-fold
91 improvement in LOD. The LODs for C≡C and C-D bonds
92 were measured by using 1,7-Octadiyne in DMSO medium
93 (Extended Data Fig. 6) and DMSO-d6 in DMSO medium
94 (Extended Data Fig. 7). In both cases, SRP showed
95 superior sensitivity than SRS with conserved average
96 power.

97 Such sensitivity improvement allows high-quality imaging
98 of nanoparticles. With the SRP microscope, we
99 successfully acquired hyperspectral image of 100 nm
100 Poly(methyl methacrylate) (PMMA) beads as shown in
101 **Fig. 3c**. The acquired SRP spectrum showed Raman
102 peak of PMMA at 2950 cm^{-1} which was well-distinguished
103 from the background spectrum as shown in Extended
104 Data Fig. 8, with an SNR ~7.0 after BM4D denoising⁴¹. In
105 comparison, the SRS measurement showed no contrast
106 of 100 nm beads on the same sample with identical
107 average laser power. Collectively, SRP showed
108 significantly improved sensitivity comparing to SRS, both
109 for liquid samples and for nanoparticles. Importantly, the
110 introduction of a third probe beam at a shorter wavelength
111 helped improve the spatial resolution (**Fig. 3d**). We
112 plotted the intensity profile across a pair of 100 nm PMMA
113 beads, with the Gaussian fitted FWHM found to be ~218
114 nm. Deconvolution with the beads size generated a
115 FWHM of ~194 nm, which was below the theoretical
116 resolution limit of SRS under the same condition (~217

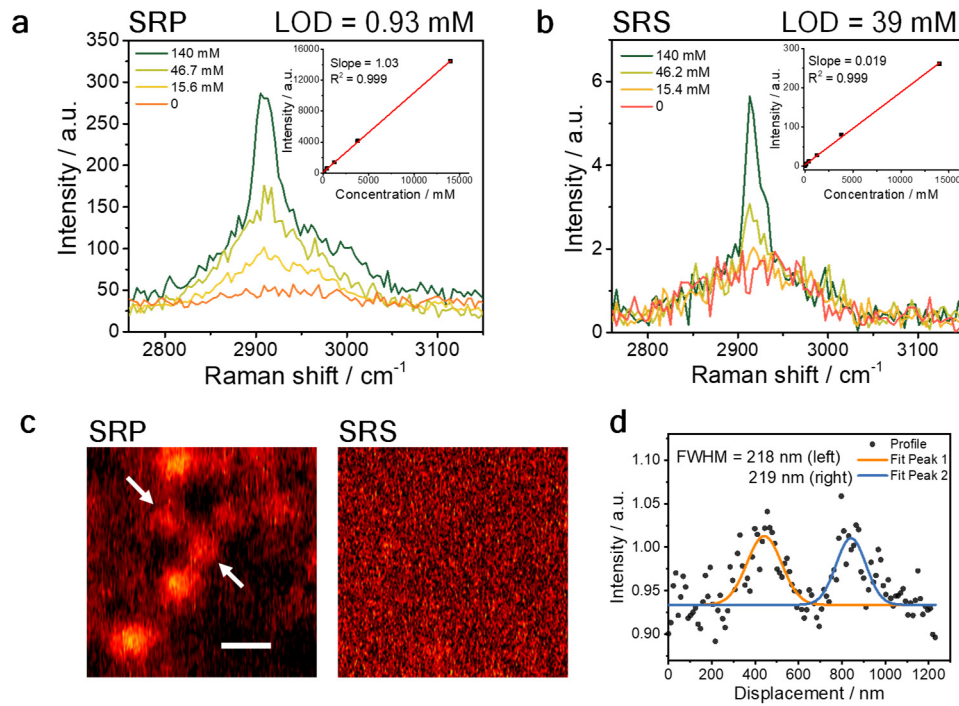


Fig. 3 SRP spectroscopy, imaging sensitivity, and spatial resolution characterization. a-b. SRP (a) and SRS (b) spectra of DMSO dissolved in DMSO-d6. Concentration unit: mM. Insert shows the signal intensity as a function of concentration (complete data in Extended Data Fig. 5). c. SRP and SRS image

of 100 nm PMMA beads at 2950 cm^{-1} with the same average power and at the same field of view. Scale bar: 500 nm. d. The Gaussian fitting of the beads indicated by arrows in panel c. FWHM: full width at half maximum.

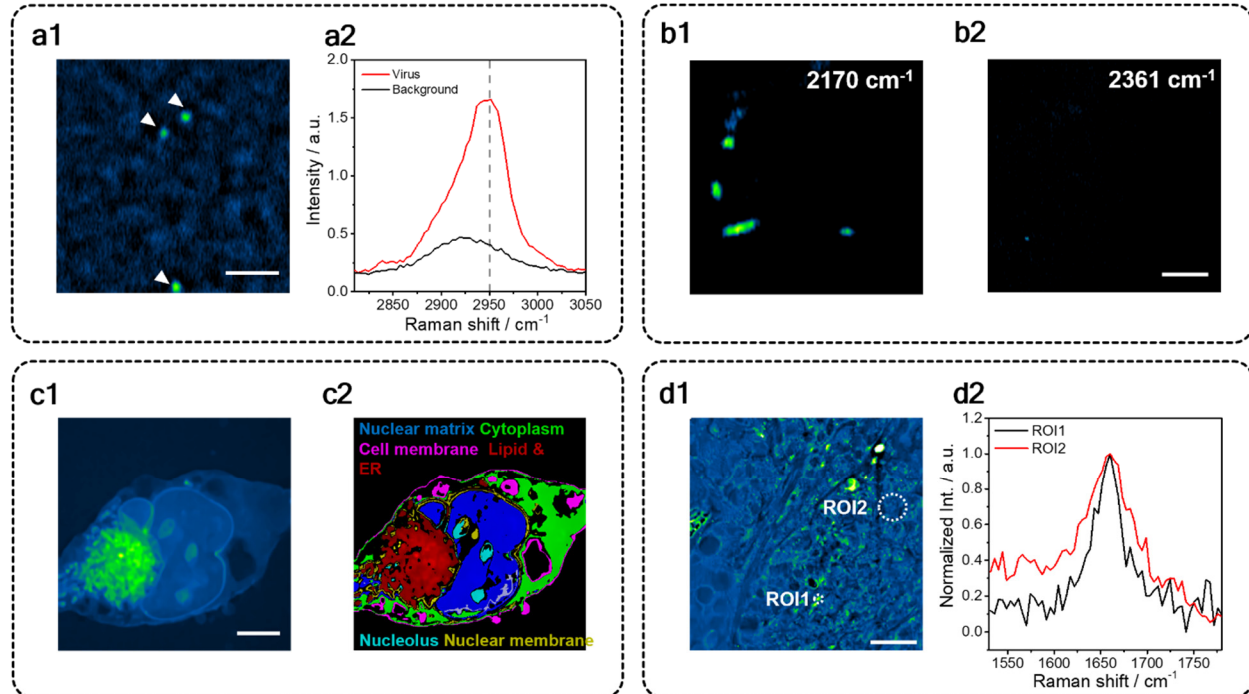


Fig. 4 Bio-applications of SRP spectroscopic imaging. a1. SRP imaging of single varicella-zoster virus, 2950 cm^{-1} . Scale bar: 2 μm . a2. Single virus SRP spectrum at the C-H region, acquired from a single virus in a1. b. C-D SRP imaging of heavy water cultured Bacteroides at 2170 cm^{-1} (b1. On-resonance) or 2361 cm^{-1} (b2. Off-resonance). Scale bar: 3 μm . c1. SRP image

of a fixed Mia-Paca2 cell immersed in glycerol-d8, at 2950 cm^{-1} . Scale bar: 5 μm . c2. Color coded chemical map through manual phasor segmentation of c1. d1. SRP spectroscopic imaging of OVCAR-5 tissue, cleared with glycerol-d8, at 1650 cm^{-1} . d2. Single pixel spectrum at the circled region of interests (ROI).

nm, FWHM of Airy disk). The FWHM was a little larger than the theoretical resolution limit yielded from the product of pump, Stokes and probe point spread functions (~167 nm), probably due to the imperfect overlap between the probe and the SRS focus along the axial axis.

Biological applications

The outstanding performance encouraged us to explore the potential of SRP in bio-imaging. Inspired by the sensitive imaging on 100-nm nanoparticles, we first tested the capability of imaging viral particles. As shown on **Fig. 4a1**, single varicella-zoster virus (diameter ≈ 180 nm)⁴² could be clearly resolved from the background with an SNR ~ 20 . The SRP spectrum of a single virus (**Fig. 4a2**) peaked at 2950 cm^{-1} , indicating strong contribution from the nucleotide at the core of the virus.

We then applied SRP microscopy to the spectrally silent region. Bacteroides cultured in heavy water were imaged as shown in **Fig. 4b1**. Decent contrast was obtained from the C-D vibration, while the off-resonance image (**Fig. 4b2**) showed little signal at the same field of view, confirming the Raman origin of the signals. Such results indicate the potential of SRP in metabolic imaging of single bacteria.

Pancreatic cancer cell MIA Paca-2 was selected as the testbed for mammalian cell imaging (**Fig. 4c1**). Glycerol-d8 was applied to replace the PBS buffer and immerse the cells to enhance the SRP contrast. SRP provided nice contrast at the C-H region. Phasor analysis was applied to segment the cellular compartments (Extended Data Fig. 9), where up to 6 different components could be well identified (**Fig. 4c2**). Notably, the nuclear membrane outstood from the cytoplasm and the nuclear matrix, giving rise to the potential of applying SRP to study fine structure in a membrane. The high contrast is probably due to the high thermo-optic coefficients and low heat capacities of membranes.

The high sensitivity of SRP also provides access to weak Raman bands in the fingerprint region. **Fig. 4d1** showed the SRP image of a $10\text{ }\mu\text{m}$ thick OVCAR-5 cancer tissue at 1650 cm^{-1} , targeting the Amide I band in proteins and the C=C vibration in lipids. High-quality spectra were resolved from the hyperspectral image stack. Lipid (region of interests 1 (ROI1)) and protein (ROI2) species are clearly differentiated, as shown in **Fig. 4d2**. Collectively, versatile bio-imaging applications are demonstrated, scaling from single virus to cancerous tissues.

1. Freudiger, C. W. *et al.* Label-free biomedical imaging with high sensitivity by stimulated Raman scattering microscopy. *Science* **322**, 1857–1861 (2008).

2. Min, W., Freudiger, C. W., Lu, S. & Xie, X. S. Coherent nonlinear optical imaging: beyond fluorescence microscopy. *Annu. Rev. Phys. Chem.* **62**, 507–530 (2011).

3. Cheng, J.-X. & Xie, X. S. Vibrational spectroscopic imaging of living systems: An emerging platform for biology and medicine. *Science* **350**, aaa8870 (2015).
4. Liao, C.-S. *et al.* Microsecond scale vibrational spectroscopic imaging by multiplex stimulated Raman scattering microscopy. *Light Sci. Appl.* **4**, e265 (2015).
5. Zhao, Z., Shen, Y., Hu, F. & Min, W. Applications of vibrational tags in biological imaging by Raman microscopy. *The Analyst* **142**, 4018–4029 (2017).
6. Ji, M. *et al.* Rapid, Label-Free Detection of Brain Tumors with Stimulated Raman Scattering Microscopy. *Sci. Transl. Med.* **5**, 201ra119 (2013).
7. Orringer, D. A. *et al.* Rapid intraoperative histology of unprocessed surgical specimens via fibre-laser-based stimulated Raman scattering microscopy. *Nat. Biomed. Eng.* **1**, 0027 (2017).
8. Hu, F. *et al.* Vibrational Imaging of Glucose Uptake Activity in Live Cells and Tissues by Stimulated Raman Scattering. *Angew. Chem. Int. Ed.* **54**, 9821–9825 (2015).
9. Shi, L. *et al.* Optical imaging of metabolic dynamics in animals. *Nat. Commun.* **9**, 2995 (2018).
10. Li, J. & Cheng, J.-X. Direct visualization of de novo lipogenesis in single living cells. *Sci. Rep.* **4**, 6807 (2014).
11. Yue, S. *et al.* Cholesteryl Ester Accumulation Induced by PTEN Loss and PI3K/AKT Activation Underlies Human Prostate Cancer Aggressiveness. *Cell Metab.* **19**, 393–406 (2014).
12. Du, J. *et al.* Raman-guided subcellular pharmacometabolomics for metastatic melanoma cells. *Nat. Commun.* **11**, 4830 (2020).
13. Lee, H. J. *et al.* Multimodal Metabolic Imaging Reveals Pigment Reduction and Lipid Accumulation in Metastatic Melanoma. *BME Front.* **2021**, 1–17 (2021).
14. Chen, C. *et al.* Multiplexed live-cell profiling with Raman probes. *Nat. Commun.* **12**, 3405 (2021).
15. Tan, Y. *et al.* Metabolic reprogramming from glycolysis to fatty acid uptake and beta-oxidation in platinum-resistant cancer cells. *Nat. Commun.* **13**, 4554 (2022).
16. Ge, X. *et al.* SRS-FISH: A high-throughput platform linking microbiome metabolism to identity at the single-cell level. *Proc. Natl. Acad. Sci. U. S. A.* **119**, e2203519119 (2022).
17. Zhang, M. *et al.* Rapid Determination of Antimicrobial Susceptibility by Stimulated Raman Scattering Imaging of D2O Metabolic Incorporation in a Single Bacterium. *Adv. Sci.* **7**, 2001452 (2020).
18. Rock, W., Bonn, M. & Parekh, S. H. Near shot-noise limited hyperspectral stimulated Raman scattering spectroscopy using low energy lasers and a fast CMOS array. *Opt. Express* **21**, 15113–15120 (2013).
19. Andrade, R. B. de *et al.* Quantum-enhanced continuous-wave stimulated Raman scattering spectroscopy. *Optica* **7**, 470–475 (2020).
20. Xu, Z. *et al.* Quantum-enhanced stimulated Raman scattering microscopy in a high-power regime. *Opt. Lett.* **47**, 5829–5832 (2022).
21. Wei, L. *et al.* Super-multiplex vibrational imaging. *Nature* **544**, 465–470 (2017).
22. Wei, L. & Min, W. Electronic Preresonance Stimulated Raman Scattering Microscopy. *J. Phys. Chem. Lett.* **9**, 4294–4301 (2018).
23. Zhuge, M. *et al.* Ultrasensitive Vibrational Imaging of Retinoids by Visible Preresonance Stimulated Raman Scattering Microscopy. *Adv. Sci.* **8**, 2003136 (2021).
24. Zong, C. *et al.* Plasmon-enhanced stimulated Raman scattering microscopy with single-molecule detection sensitivity. *Nat. Commun.* **10**, 5318 (2019).
25. Xiong, H. *et al.* Stimulated Raman excited fluorescence spectroscopy and imaging. *Nat. Photonics* **13**, 412–417 (2019).
26. Wang, H., Fu, Y. & Cheng, J.-X. Experimental observation and theoretical analysis of Raman resonance-enhanced photodamage in coherent anti-Stokes Raman scattering microscopy. *J. Opt. Soc. Am. B* **24**, 544 (2007).
27. Adhikari, S. *et al.* Photothermal Microscopy: Imaging the Optical Absorption of Single Nanoparticles and Single Molecules. *ACS Nano* **14**, 16414–16445 (2020).
28. Gaiduk, A., Yorulmaz, M., Ruijgrok, P. V. & Orrit, M. Room-Temperature Detection of a Single Molecule's Absorption by Photothermal Contrast. *Science* **330**, 353–356 (2010).
29. Long, M. E., Swofford, R. L. & Albrecht, A. C. Thermal Lens Technique: A New Method of Absorption Spectroscopy. *Science* **191**, 183–185 (1976).

30. Zhang, D. *et al.* Depth-resolved mid-infrared photothermal imaging of living cells and organisms with submicrometer spatial resolution. *Sci. Adv.* **2**, e1600521 (2016).
31. Li, Z., Aleshire, K., Kuno, M. & Hartland, G. V. Super-Resolution Far-Field Infrared Imaging by Photothermal Heterodyne Imaging. *J. Phys. Chem. B* **121**, 8838–8846 (2017).
32. Fu, P. *et al.* Super-resolution imaging of non-fluorescent molecules by photothermal relaxation localization microscopy. *Nat. Photon.* 1–8 (2023)
33. El-Kashef, H. The necessary requirements imposed on polar dielectric laser dye solvents—II. *Phys. B Condens. Matter* **311**, 376–379 (2002).
34. Bowen, E. J. & Sahu, J. The Effect of Temperature on Fluorescence of Solutions. *J. Phys. Chem.* **63**, 4–7 (1959).
35. Soleilhac, A. *et al.* Temperature Response of Rhodamine B-Doped Latex Particles. From Solution to Single Particles. *Langmuir* **32**, 4052–4058 (2016).
36. Li, M. *et al.* Fluorescence-Detected Mid-Infrared Photothermal Microscopy. *J. Am. Chem. Soc.* **143**, 10809–10815 (2021).
37. Zhang, Y. *et al.* Fluorescence-Detected Mid-Infrared Photothermal Microscopy. *J. Am. Chem. Soc.* **143**, 11490–11499 (2021).
38. Freudiger, C. W. *et al.* Stimulated Raman scattering microscopy with a robust fibre laser source. *Nat. Photonics* **8**, 153–159 (2014).
39. Gaiduk, A., Ruijgrok, P. V., Yorulmaz, M. & Orrit, M. Detection limits in photothermal microscopy. *Chem. Sci.* **1**, 343–350 (2010).
40. Novais, S., Ferreira, M. S. & Pinto, J. L. Determination of thermo-optic coefficient of ethanol-water mixtures with optical fiber tip sensor. *Opt. Fiber Technol.* **45**, 276–279 (2018).
41. Maggioni, *et al.*, A. Nonlocal transform-domain filter for volumetric data denoising and reconstruction. *IEEE Trans Image Process* **22**, 119–133 (2013).
42. Sauerbrei, A. Diagnosis, antiviral therapy, and prophylaxis of varicella-zoster virus infections. *Eur. J. Clin. Microbiol. Infect. Dis.* **35**, 723–734 (2016).

Methods

Modeling the temperature change induced by SRS

To quantitatively evaluate the SRP effect, we built a model to simulate the heat deposition spatially and temporally. The SRS induced temperature change is dependent on the pulse width, the pulse energy, laser repetition rate, and the thermal properties (thermal conductivity, heat capacity, etc.) of the sample and the surrounding medium. First, the deposited energy by SRS is estimated by the modulation depth on pump or Stokes beam along with the pulse energy. Then, to simulate the thermal conduction, the time domain and spatial domain are divided to finite elements for the calculation according to the Fourier's law: $dQ = -kA(dT/dr)$, where dQ is the conducted heat energy in the time window, k is the thermal conductivity, A is the surface area, dT is the temperature difference between distance dr . The SRS on-off process induces a heating and cooling process at the focus. The heat transfer happens during both heating and cooling. During the heating process, the SRS pulses deposit heat to the sample instantaneously with a Gaussian distribution as the vibrational excited state relaxation time is much faster compared to the simulation time grid. Finally, with the heating estimated by the modulation depth and the thermal conduction calculated according to the Fourier's Law, the temperature spatial distribution at each time point is calculated.

To simplify the model, an isotropic Gaussian SRS heating area is assumed. The simulation area is set to be a 48-layer model with increasing step size from center to the edge (Extended Data Fig. 1). Time step is set to be 200 ps, which is much smaller than the heat propagation time to ensure a converge result. DMSO has a heat conductivity of 0.2 W/(m·K). The laser parameters are set to 50% duty cycle, 80 MHz repetition rate, according to the commonly used SRS setting.

To predict the fluorescence change upon temperature rise, the excitation profile of two photon fluorescence was modeled as the normalized Gaussian point spread function of the objective. Weights based on the assumed excitation profile were put onto the temperature rise of each layer, then multiplied by the $-2\%/K$ rate³⁴, to yield the fluorescence change.

Measurement of temperature at the SRS focus

A fluorescence thermometer, Rhodamine B ($-2\%/K$)³⁴, is introduced to measure the temperature rise at the SRS focus. 80 μ M Rhodamine B dissolved in DMSO is sandwiched between two thin coverslips (No.1; Thermo Fisher) for the measurement. A dual-output synchronized laser source (InSight X3; Spectra-Physics) provides pump and Stokes beams, respectively. The Stokes beam is modulated by an acousto-optic modulator (1205c; Isomet Corporation) at 40 kHz with the first order beam to provide a 100% modulation depth. Then the pump and Stokes beams are chirped by 75 and 90 cm glass rods (SF57; Scott AG), respectively, to implement hyperspectral SRS under a spectral focusing scheme. The path length of the Stokes beams could be adjusted

by a motorized delay line (X-LRM025A-KX13A, Zaber Technologies). The two beams are combined by a dichroic mirror (950 nm; Chroma) and then collinearly guided into a laser scanning microscope. To vibrationally excite the C-H bond in DMSO, the pump laser was set to 800 nm with the Stokes beam wavelength fixed at 1045 nm. These two beams could also simultaneously excite the two-photon fluorescence signal of Rhodamine B. A 40 \times water objective (numerical aperture (N.A.) = 0.8; Olympus) focused the two beams onto the sample, with power of 25 mW for pump and 50 mW for Stokes. The output light is collected in the forward direction by an oil condenser (N.A. = 1.4, Aplanat Achromat 1.4; Olympus) and a 75 mm A-coating focal lens (Thorlabs). A silicon photomultiplier (C14455-3050GA; Hamamatsu) module with a bandpass optical filter (RT570/20x; Chroma) and two short-pass filters (1000SP, 775SP; Thorlabs) is used to detect the fluorescence signal. The output of the silicon photomultiplier is recorded by a spectrometer (Moku:Lab, Liquid Instruments) for the analysis in Fig. 1f.

SRP microscope

The SRP microscope is based on the SRS setup described in the previous section. Both pump and Stokes beams are modulated by two synchronized acousto-optic modulators outputting the first order beams, various duty cycles, and modulation frequency at 125 kHz. Besides, a 765 nm continuous probe laser (TLB6712-D; Spectral Physics) is added after the combining dichroic mirror by a polarized beam splitter to form a three beam copropagating colinear system (Fig. 2b). The three beams are guided to a two-dimensional galvo scanning unit (GVS002; Thorlabs), which is conjugated by a four-focal system to the back aperture of a 100 \times oil objective (N.A. = 1.49, UAPON100XOTIRF; Olympus). The N.A. of the condenser is adjusted to 0.4 to enable the detection of the thermal lensing signal. The detector is a broadband silicon photodiode (Hamamatsu) with 50-ohm resistance, a 22 kHz highpass radio frequency filter (Mini-circuits) and a 46 dB low noise amplifier (SA230-F5; Wayne). A tilted bandpass optical filter (FL780-10; Thorlabs) is mounted before on the detector to block the SRS beams and allow sole detection of the probe beam. The output signal is digitized by a fast data acquisition card (Alazar card, ATS9462; Alazar Technologies). In imaging the virus on a coverslip, the 1045-nm femtosecond laser output is sent to an LBO crystal to generate 522.5-nm laser beam as the SRP probe. This femtosecond probe with reduced coherence length minimizes the interference from the medium / coverglass interface.

When performing SRS imaging on the same setup, the probe laser is turned off. A 1.4 N.A. condenser is used to minimize the cross phase modulation background. The modulation on pump is set to always on and the Stokes was modulated at around 2.25 MHz. After the condenser, two short-pass optical filters (980SP, Thorlabs) pass the pump beam to the photodiode. A laboratory-built resonant amplifier after the photodiode picks up the stimulated Raman loss signal. The photodiode output is sent to the lock-in amplifier (MFLI; Zurich) and the

stimulated Raman loss signal is recorded with a dataacquisition card (NI DAQ card, PCI-6363; National Instruments). The SRP system is electronically synchronized by a NI DAQ card. The NI DAQ card controls the galvo scanning unit and generates the transistor-transistor logic trigger to control the sampling of the Alazar card and the pixel trigger to control the function generator. The function generator generates rectangular waves with various duty cycle at 125 kHz in burst mode to control the two acousto-optic modulators to modulate the pump and Stokes pulse trains (Extended Data Fig. 2). The amplified signal from the detector set is digitized by the Alazar card at a sampling frequency of 20 MHz and then sent to the host computer for further analyze.

SRP signal digitization and processing After recording the signal from each pixel, a Whittaker smoother removes the fluctuated baseline caused by variation in the transmission⁴³. Matched filtering is then applied to improve the SNR⁴⁴. Fourier transform on the baseline removed signal is applied to generate the signal spectrum. To reduce the out-of-frequency noise, a match multi-bandpass filter at the up to seven harmonic frequencies of the modulation frequency is applied to the signal spectrum (Extended Data Fig. 3). The width of single bandpass filter is set to 13.89 kHz when the pixel dwell time is 72 μ s. The match-filtered spectrum is then inversely Fourier transformed back to the time domain. The SPR signal intensity of each pixel is calculated from the average peak-dip contrast of the processed time domain data.

Cell culture and sample preparation

SKOV3 (Cat#: HTB-77) and Mia Paca2 (Cat#: CRL-1420) cells were from the American Type Culture Collection (ATCC). Cells were cultured in high-glucose DMEM medium (Gibco) supplemented with 10% FBS and 100 units/mL penicillin/streptomycin and maintained in a humidified incubator with 5% CO₂ supply at 37°C. After overnight seeding in a sterile 35 mm glass-bottom dishes (Cellvis) or #1 cover glass (VWR), cells were fixed with 10% neutral buffered formalin for 30 min followed by 3 times PBS wash. Then the cells were covered with glycerol-d8 before sealing and imaging.

Tissue sample preparation

A fresh ovarian tumor section was extracted from NU/J mouse (4 weeks old female homozygous for Foxn1nu) purchased from the Jackson Laboratory. The mouse was inoculated with OVCAR5-cisR cells. The sections were immediately fixed in a 10% formalin solution. The extracted tissue section was then washed using PBS solution and cryopreserved by incubation in 15% sucrose solution for 12 hours, followed by incubation in 30% sucrose solution overnight at room temperature. The tissue section was frozen at -80°C by embedding in OCT (Optimal Cutting Temperature) compound in a tissue mold. The tissue section was then sliced using a Microm HM525 cryostat at the Bio-Interface and Technologies

Facility, Boston University, into 10 μ m thick layers, each placed on separate glass slides and frozen at -80°C until the experiment. To prepare the samples for imaging, the tissue slides were washed using PBS solution to wash off the OCT. The tissue slides were then covered with glycerol-d8 before placing a coverslip to seal the glycerol-d8 covered tissue layer.

Glycerol-agar (glycerol-d8-agar) medium preparation

1% (w/w) agar (Sigma Aldrich) was mixed with glycerol (or glycerol-d8, Sigma Aldrich), then microwaved for 2min to fully dissolve the agar.

Nanoparticle, bacteria, and virus preparation

For 100 nm PMMA nanoparticles, 10 μ L solution was mixed with warm glycerol-d8-agar medium, then sandwiched between two No.1 coverslips before imaging. For D₂O cultured bacteroid¹⁶, 10 μ L solution of fixed bacteria was mixed with warm glycerol-agar medium, then sandwiched between two No.1 coverslips before imaging. Varicella zoster virus solution (Fisher Scientific) was dropped onto a No.1 coverslip and dried on top. The sample was covered with glycerol-d8, then sandwiched between two coverslips and sealed with nail polish before imaging.

SRP imaging parameters

The modulation depth is measured with 5% duty cycle modulation, 50 mW and 20 mW for Stokes and pump, respectively. The virus image is acquired with 5% duty cycle modulation, 40 mW and 20 mW for Stokes and pump, respectively. The bacteria image is acquired with 10% duty cycle modulation, 30 mW and 20 MW for Stokes and pump, respectively. The cell image is acquired with 10% duty cycle modulation, 30 mW and 15 mW for Stokes and pump, respectively. The tissue image is acquired with 5% duty cycle modulation, 30 mW and 10 mW for Stokes and pump, respectively. All powers are measured before the microscope.

Phasor analysis

Phasor analysis was performed with the standardized phasor analysis plug-in in ImageJ (1.49v). The phasor domain segmentation was performed manually to maximize the separation of different components as well as the integrity of each component.

43. Eilers, P. H. C. A perfect smoother. *Anal. Chem.* **75**, 3631–3636 (2003).

44. Yin, J. *et al.* Nanosecond-resolution photothermal dynamic imaging via MHz digitization and match filtering. *Nat. Commun.* **12**, 7097 (2021).

45. Bialkowski, S. E., "Photothermal spectroscopy methods for chemical analysis" in *Chemical Analysis: A Series of Monographs on Analytical Chemistry and Its Applications*, J. D. Winefordner, ed., (John Wiley & Sons, Inc., 1996), Vol. **13A**.

46. Cao, Z. *et al.* All-glass extrinsic Fabry-Perot interferometer thermo-optic coefficient sensor based on a capillary bridged two fiber ends. *Appl. Opt.* **54**, 2371–2375 (2015).

Data Availability

All data are available upon reasonable request to the corresponding author (jxcheng@bu.edu(J.X.C.)).

Code Availability

The image reconstruction codes are available upon reasonable request to the corresponding author (jxcheng@bu.edu (J.X.C.)).

Acknowledgements

Department Boston University for assisting with preparation of cancer cells and tissues. We thank Fátima C. Pereira from Centre for Microbiology and Environmental Systems Science University of Vienna for assisting with preparation of bacterial cells. This work is supported by R35GM136223 to J.X.C. We thank Yuying Tan from Biomedical Engineering

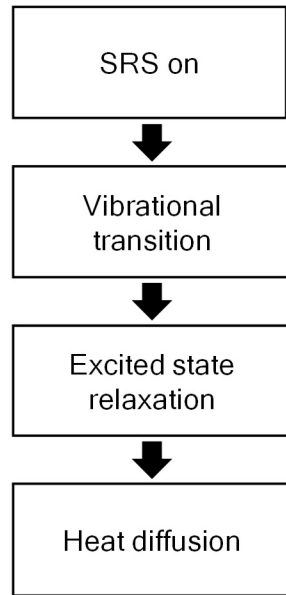
Author contributions

J.X.C. conceived the concept of photothermal detection and supervised the research team; Y.Z. built the simulation model, designed and built the SRP imaging system; X.G. implemented the data analysis algorithm; Y.Z. and X.G. performed the imaging experiments and data analysis; J.Y. designed and implemented the matched filtering algorithm; H.N. designed and implemented the broadband detector; Y.Z., X.G. and J.X.C. wrote the manuscript with input from all authors.

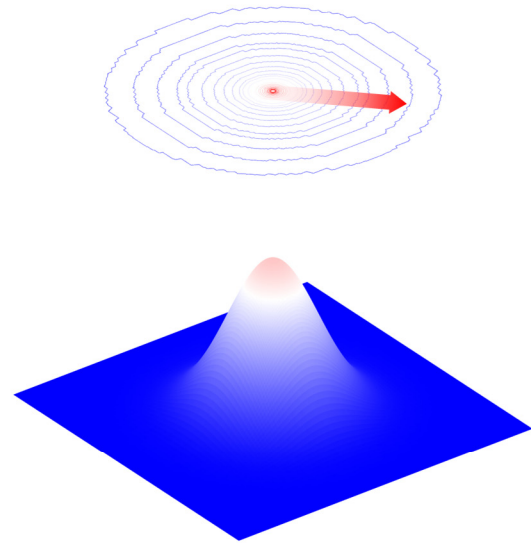
Competing interests

J.X.C. declares financial interests in Vibronix Inc. and Photothermal Spectroscopy Corp., which did not fund the study.

a.

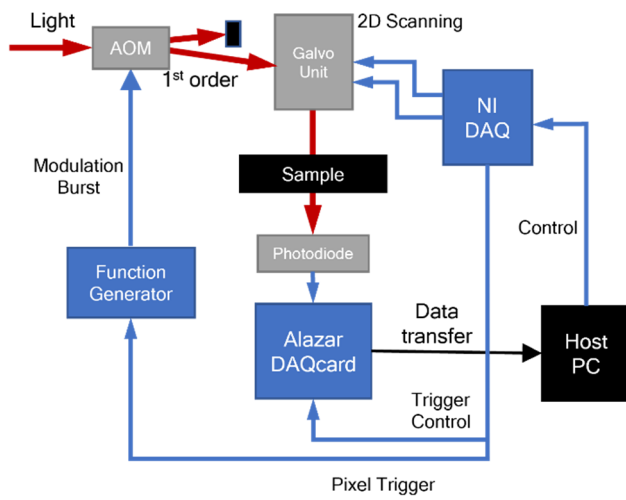


b.

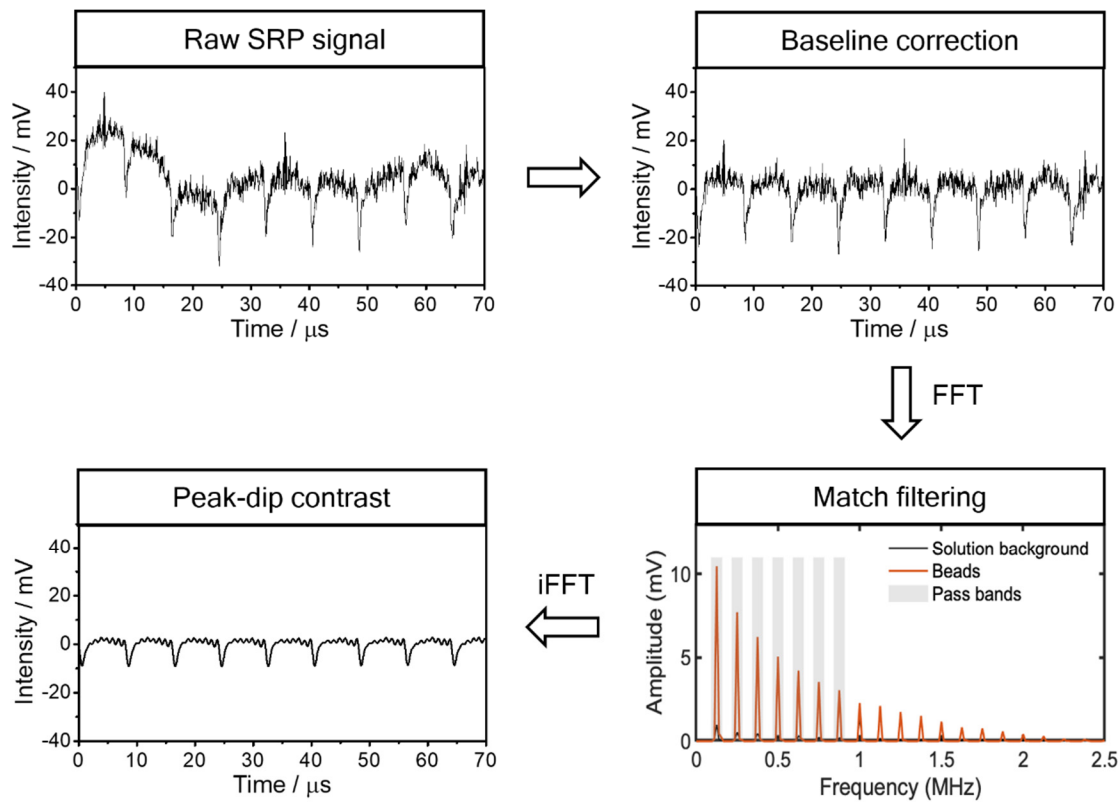


$$dQ = -kA \frac{dT}{dr} = -k(4\pi r^2) \frac{dT}{dr}$$

Extended Data Figure 1. SRP simulation model. The system is meshed into concentric spherical shells. The red arrow indicates the thermal propagation direction.



Extended Data Figure 2. Electronic control and data acquisition flow in the SRP microscope.

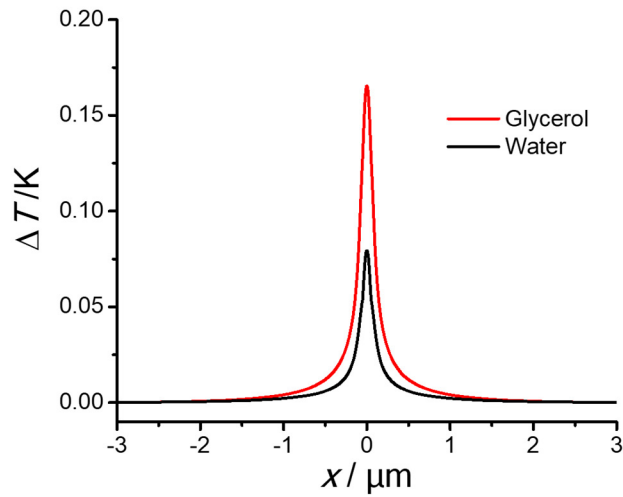


Extended Data Figure 3. A thermal dynamic trace from SRP measurement and under different stages of data processing. Signal is acquired from a single 100 nm PMMA nanoparticle at 2950 cm^{-1} immersed in glycerol-d₈. FFT: fast Fourier transform; iFFT: inverse fast Fourier transform.

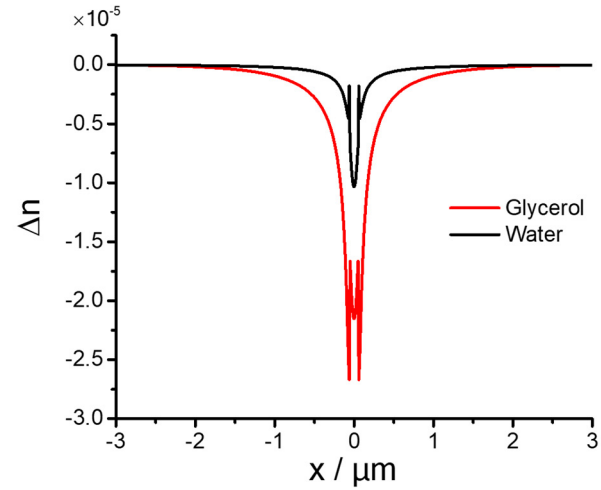
Thermal property	Unit	DMSO	hexane	glycerol	water
Heat Capacity	J/(kg·K)	1966	2251	2400	4184
Thermal conductivity	W/(m·K)	0.200	0.124	0.283	0.598
Thermo-optic coefficient dn/dT (10 ⁻⁴)	K ⁻¹	-4.93 ³³	-5.20 ⁴⁵	-2.30 ⁴⁶	-1.13 ⁴⁰
Refractive index		1.479	1.375	1.473	1.333
Relative signal intensity	a.u.	10.3	8.83	4.27	1

Extended Data Table 1. Thermal and thermo-optic properties and estimated relative signal intensity of the mediums related to the study.

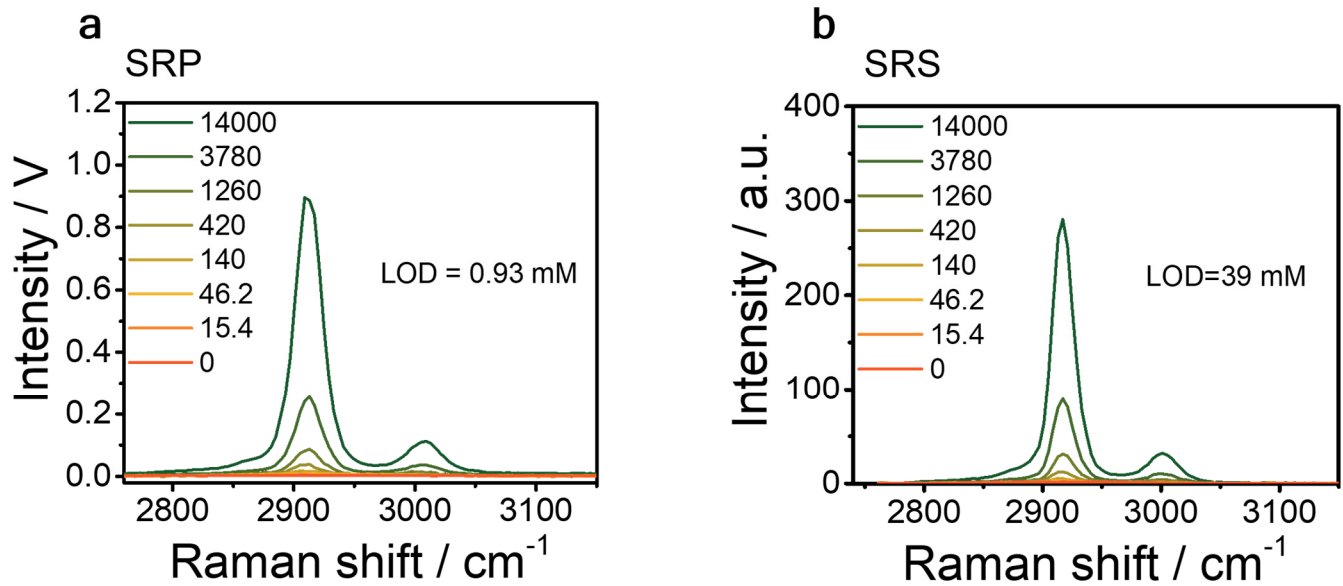
Temperature gradient



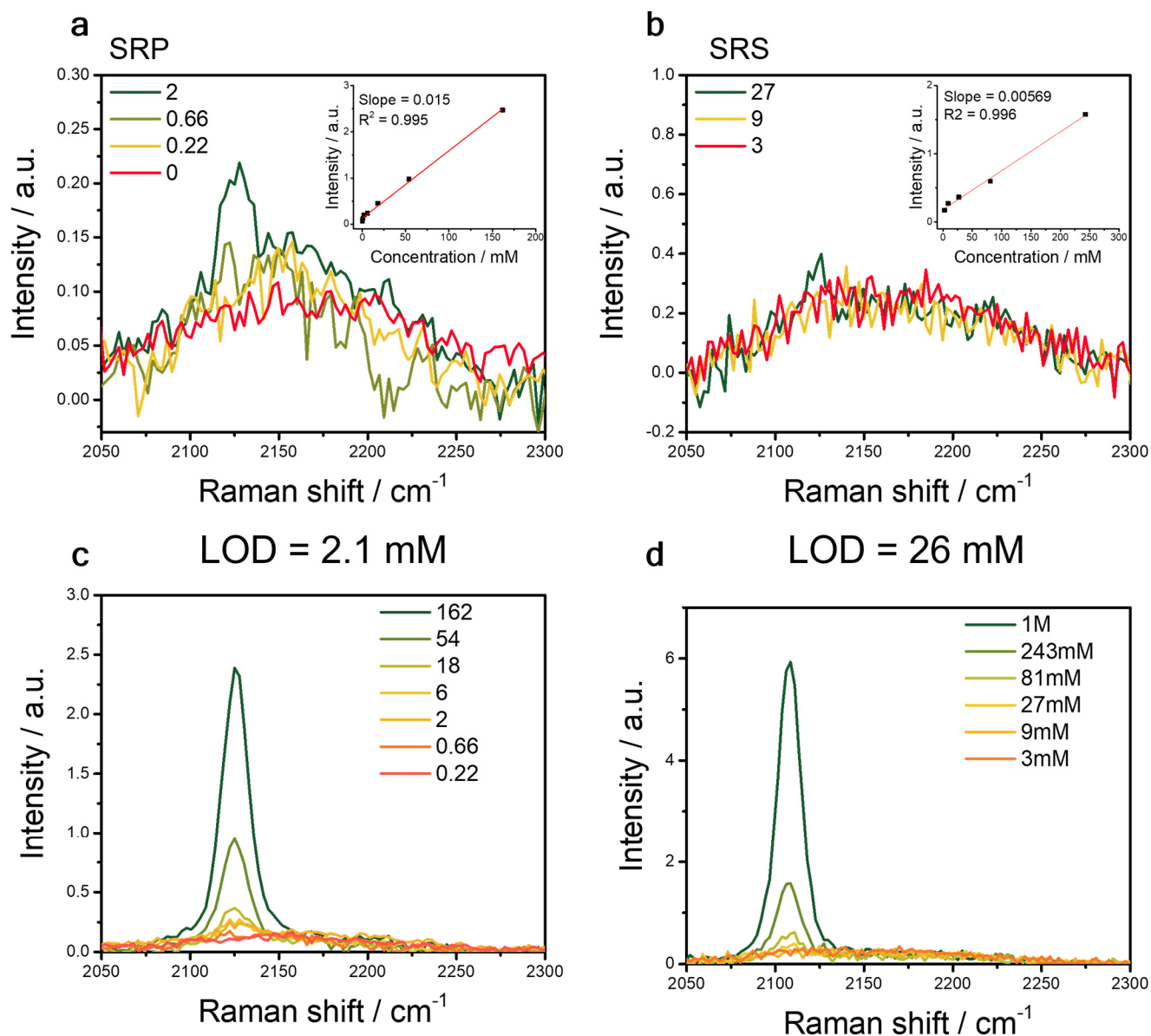
Shape of thermal lens



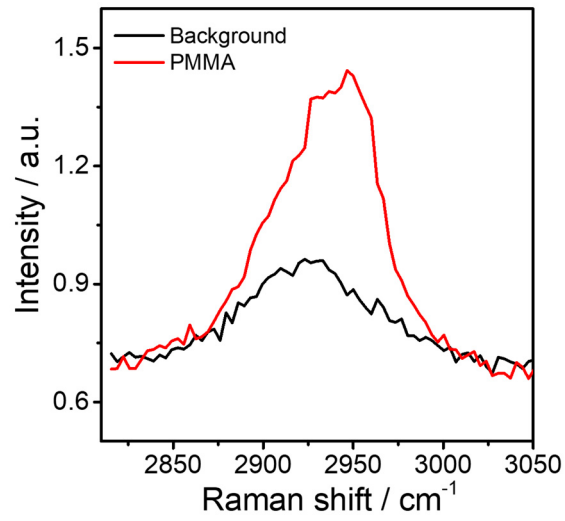
Extended Data Figure 4. Simulation results for the shape of temperature gradient and thermal lens induced by a 100 nm PMMA particle in glycerol or water.



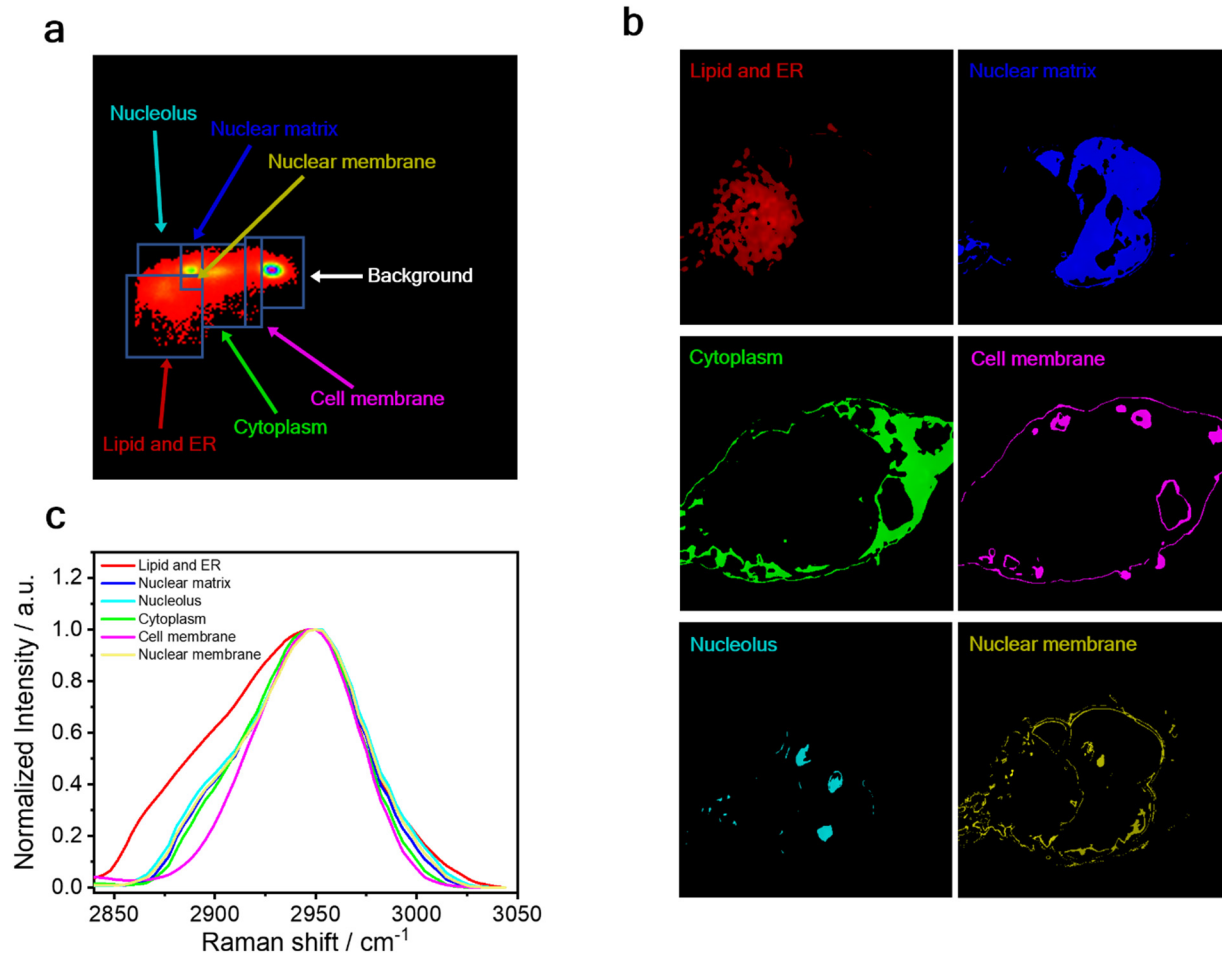
Extended Data Figure 5. Complete data set of LOD measurement of DMSO dissolved in DMSO-d6 with SRP (a) and SRS (b). Unit of concentration: mM.



Extended Data Figure 6. LOD of 1,7-Octadiyne in SRP and SRS measurement. a-b. SRP (a) or SRS (b) signal with gradient concentration of 1,7-Octadiyne dissolved in DMSO. Concentration unit: mM. Insert shows the signal intensity as a function of concentration. **c-d.** Complete data set of LOD measurement with SRP (c) and SRS (d). Unit of concentration: mM.



Extended Data Figure 8. SRP spectrum of a single 100 nm PMMA nanoparticle at the C-H region.



Extended Data Figure 9. Phasor analysis for the SRP image of glycerol-d8 immersed Mia PACA-2 cells. a. Segmentation of the SRP image in phasor domain. **b.** Mapping of each component from phasor analysis. **c.** The SRP spectrum at C-H region for each component.